A Journal of the Gesellschaft Deutscher Chemiker

Angewandte International Edition GDCh Chemie

www.angewandte.org

Accepted Article

Title: Versatile Nickel (II) Scaffolds as Coordination-Induced Spin-State Switches for 19F Magnetic Resonance-Based Detection

Authors: Da Xie, Meng Yu, Zhu-Lin Xie, Rahul T. Kadakia, Chris Chung, Lauren E Ohman, Kamyab Javanmardi, and Emily Lauren Que

To be cited as: *Angew. Chem. Int. Ed.* 10.1002/anie.202010587

Link to VoR: https://doi.org/10.1002/anie.202010587

WILEY-VCH

10.1002/anie.202010587

WILEY-VCH

RESEARCH ARTICLE

Versatile Nickel (II) Scaffolds as Coordination-Induced Spin-State Switches for ^{19}F Magnetic Resonance-Based Detection

Da Xie[a], Meng Yu[a], Zhu-Lin Xie[a], Rahul T. Kadakia[a], Chris Chung[a], Lauren Ohman[a], Kamyab Javanmardi[b], Emily L. Que*[a]

Abstract: ^{19}F magnetic resonance-based detection coupled with well-designed inorganic systems shows great promise in biological investigations including metabolic tracking, studies of protein structure and function, molecular imaging, and medical diagnostics, providing low biological background and high specificity of the modality. Two proof-of-concept inorganic probes are reported that exploit a novel mechanism for ^{19}F MR sensing based on converting from low-spin (S=0) to high-spin (S=1) Ni^{2+}. Activation of diamagnetic **NiL$_1$** and **NiL$_2$** via light or β-galactosidase respectively converts them into paramagnetic **NiL$_0$** that displays a single ^{19}F NMR peak shifted by >35 ppm with accelerated relaxation rates. This large chemical shift change is facilitated by contact and pseudo-contact interactions between the ^{19}F reporter and the 5-coordinate Ni^{2+}. This spin-state switch is effective for sensing light or enzyme expression in live cells using ^{19}F MR spectroscopy and imaging that differentiate signals based on chemical shift and relaxation times. This general inorganic scaffold has potential for developing agents that can sense analytes ranging from ions to enzymes, opening up diverse possibilities for ^{19}F MR-based biosensing.

Introduction

The magnetic properties of metal complexes can be applied in a number of contexts ranging from data storage[1] to medical diagnostics[2]. One exciting frontier is in biosensing, where the magnetism of metal complexes can be exploited and manipulated to develop smart scaffolds for reporting unique physiochemical and biochemical signatures in living systems.[3] ^{19}F magnetic resonance techniques including spectroscopic (^{19}F nuclear magnetic resonance spectroscopy, NMR/MRS) and imaging modalities (^{19}F magnetic resonance imaging, MRI) are promising techniques for biosensing and medical diagnostics with excellent tissue penetration depth and high sensing specificity.[4] ^{19}F exhibits excellent MR properties with sensitivity close to ^{1}H and a large chemical shift range over 350 ppm. Further, there is no detectable endogenous signal in typical biological samples including humans; ^{19}F MR signal can be directly correlated to the concentration of fluorinated probe, enabling quantification.[5] These properties have enabled the use of ^{19}F as a unique handle for investigating at protein structure and function, tracking metabolism, and developing molecular imaging agents.[6] Combining ^{19}F magnetic resonance spectroscopy with the rich magnetic and chemical properties of metal complexes provides a diverse toolbox for the development of a diverse array of activatable probes for ^{19}F-based biosensing.

To date, multiple metal complexes have been established as probes that respond to specific biochemical processes through manipulating metal-fluorine interactions.[6c] Gd^{3+} complexes have been reported for sensing enzymatic activity.[7] In these probes, the ^{19}F MR signal is quenched due to intramolecular paramagnetic relaxation enhancement (PRE) from the Gd^{3+} and restored following enzyme-specific cleavage of the link between the Gd^{3+} and the ^{19}F reporter. Metal redox couples such as Mn^{2+}/Mn^{3+},[8] Co^{2+}/Co^{3+},[9] Cu^{+}/Cu^{2+},[10] and Eu^{2+}/Eu^{3+}[11] have also been used; in this case ^{19}F MR signatures (relaxation time and chemical shift) are modulated by altering the oxidation state and spin state of metal center in response to redox events. A third strategy is to exploit changes in donor strength to modulate metal spin state and thus ^{19}F chemical shifts including systems based on Co^{2+} [12] and Fe^{2+} [13]. A fourth design strategy is tuning the coordination number and geometry of the metal center to manipulate the magnetic properties of the complex, affording distinct ^{19}F MR signals. While lanthanide containing probes using this strategy have been reported,[14] this remains largely unexplored with transition metal complexes.

Ni^{2+} complexes have been investigated for the accessibility of both high-spin and low-spin states in an aqueous environment, dependent on the Ni^{2+} coordination geometry.[15] A square-planar Ni^{2+} almost always adopts a diamagnetic configuration (S = 0), while a five or six-coordinate Ni^{2+} favors a paramagnetic configuration (S = 1). Though paramagnetic Ni^{2+} complexes have been used as ^{19}F MR tracers for live-cell labeling, examples of spin-state-switching Ni^{2+} complexes are rare in the field of MR biosensors and have not been reported for ^{19}F.[16] Ni^{2+} azoporphyrin complexes were reported as light-induced spin-state switches for ^{1}H MRI based on coordination change, but poor aqueous solubility has limited their application in biological environments.[17]

Herein we present a versatile Ni^{2+} platform utilizing a side-bridged cyclam (1,4,8,11-tetraazacyclotetradecane) ligand that can undergo coordination-induced spin-state switch upon activation (**Figure 1**). The modularity of the sensing platform was demonstrated by two proof-of-concept probes, **NiL$_1$** and **NiL$_2$**, for sensing photoactivation and β -galactosidase activity, respectively, both forming **NiL$_0$** as product. Spectroscopic, single-

[a] D. Xie, Dr. M. Yu, Dr. Z. Xie, R.T. Kadakia, C. Chung, L. Ohman, and Prof. Dr. E.L. Que
Department of Chemistry
The University of Texas at Austin
105 E. 24th St Stop A5300, Austin, Texas 78712, United States
E-mail: emilyque@cm.utexas.edu
[b] K. Javanmardi
Department of Molecular Biosciences
The University of Texas at Austin
2500 Speedway, Austin, TX 78712, USA

Supporting information for this article is given via a link at the end of the document.

10.1002/anie.202010587
WILEY-VCH

RESEARCH ARTICLE

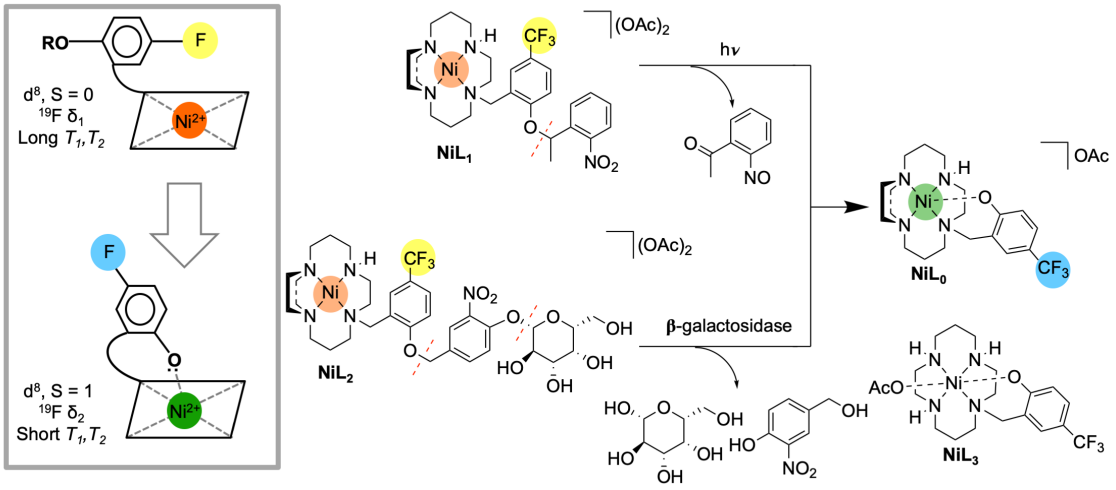

Figure 1. Design strategies (left box) and the structures and sensing mechanisms (right) of spin-state switching Ni^{2+} complexes for ^{19}F magnetic resonance biosensing.

crystal, and computational studies revealed that **NiL₁** and **NiL₂** are square planar and diamagnetic, while **NiL₀** is five- coordinate and paramagnetic. The large difference in relaxation times and chemical shift between paramagnetic (**NiL₀**) and diamagnetic species (**NiL₁** and **NiL₂**) allowed selective ^{19}F MR imaging of individual complexes in different magnetic states. The spin-flipping process was successfully assessed in solution and in cellular environments via ^{19}F MR-based techniques, thus highlighting Ni^{2+} side-bridged cyclam scaffolds as reliable and flexible platforms to develop responsive ^{19}F MR sensors.

Results and Discussion

Probe design and synthesis

To develop Ni^{2+} complexes as ^{19}F MR probes with switchable spin states based on coordination geometry, two requirements must be taken into account: (1) in the low-spin square-planar Ni^{2+} complex, access of surrounding anions or solvent molecules to Ni^{2+} center from the axial position should be minimized; otherwise it may be easily converted to the high-spin complex in biological media. (2) After probe activation, axial coordination of an intramolecular donating ligand should be strong enough to generate a high-spin Ni^{2+} complex in order to compensate the energetic penalty associated with spin-state change. Donating ligands with less steric bulk and slow ligand exchange kinetics are favored.

We chose a cyclam-based scaffold for our probes given its strong affinity for 3d transition metals and the broad application of cyclam metal complexes in biological settings.[18] The specific probe design was inspired by past studies on Ni^{2+} side-bridged-cyclam (SB-cyclam) complexes that are diamagnetic even in presence of strong coordinating anions including CN^-, SCN^- and N_3^- in aqueous solution.[19] The bis-ethylene bridge enforces planarity of the N donors and a small metal binding pocket, both of which favor a square planar, low-spin Ni^{2+}. On the other hand, although much less explored, SB-cyclam with pendant coordinating groups can accommodate high-spin Ni^{2+} ions.[20] Therefore, we envisioned to couple coordination-induced spin-state change with MR-based sensing by appending a "caged" donating ligand to Ni^{2+} SB-cyclam complexes, where the caging group will be removed after probe activation by a specific analyte (**Figure 1**). We chose a "caged" phenol due to the drastic difference of donating strength between an ether group and a phenolate. Moreover, there is literature precedent for high-spin phenolate Ni^{2+} cyclam complexes.[21] For a readily tractable proof-of-concept probe, we protected the phenol with a photo-labile *ortho*-nitrobenzyl group to afford **NiL₁**, which will undergo bond cleavage following UV-irradiation to release phenolate and form **NiL₀**. We also prepared **NiL₂** that responds to cleavage by β-galactosidase via a self-immolative process to also generate **NiL₀**. Both probes were successfully applied in live cells, opening the possibility of imaging dynamic biochemical processes in cells and beyond. This probe platform can be readily adapted to detect any analyte that can induce a specific cleavage event that transforms the coordination properties of the ligand scaffold.

Briefly, the syntheses of **NiL₁** and **NiL₂** were carried out starting from 5-trifluoromethyl-salicylaldehyde. "Activatable" groups (ortho-nitrobenzyl for **NiL₁**; nitrophenyl-β-galactoside for **NiL₂**) were attached to the phenol via S_N2 reactions with nearly quantitative yield (**Scheme S1-S3**). The formed benzaldehyde was then converted to the corresponding benzyl bromide in two steps with an overall yield of 40-50%. Following a classical synthetic procedure, protected cyclam was conjugated with the

10.1002/anie.202010587

above prepared benzyl bromide to furnish the ligand precursor as a bromide salt (64-87% yield), followed by reduction via $NaBH_4$ to produce the ligands **L_1** and **L_2** in 74% and 79% yield, respectively. The Ni^{2+} complexes were formed by heating a methanolic solution of the ligand and nickel acetate, with 87% yield for **NiL_1** and 84% yield for **NiL_2**. Perchlorate analogues were also synthesized, however these complexes were less soluble and thus were not the main focus of this study. To independently investigate the formed product, we also prepared **NiL_0** and its cyclam analogue, **NiL_3**, using synthetic route similar to **NiL_1** and **NiL_2**. Full synthetic procedures and characterizations are provided in the supporting information.

Solution behavior of NiL_1

All prepared Ni^{2+} complexes exhibited excellent aqueous solubility up to 100 mM. The UV-vis absorption spectrum of **NiL_1** in HEPES buffer (**Figure S1**) contained an absorption band centered at 480 nm (ε = 2.7x10^2 $M^{-1}cm^{-1}$), which was assigned to a spin-allowed d-d transition. This absorption feature matched with a previously reported square planar Ni^{2+} SB-cyclam complex,[20] supporting the presence of a square-planar low-spin Ni^{2+} complex in aqueous solution. We note that the extinction coefficient of **NiL_1** is slightly higher than in perfectly square planar Ni^{2+} complexes,[22] potentially indicative of a slight tetrahedral distortion of the cyclam-N_4 donors. Magnetic moment measurement of **NiL_1** determined via Evan's method confirmed the largely diamagnetic nature of the complex in the same buffer (0.51 μ_B). The slight paramagnetism is likely due to the unfavored axial access of ligands (e.g. water and anions) to the Ni^{2+}.

Interestingly, the ^{19}F NMR spectrum of **NiL_1** showed two adjacent singlet peaks (-61.53 and -61.57 ppm) separated by 18 Hz with an approximate intensity ratio of 1:1 (**Figure S2**). Given that ligand **L_1** only displayed one singlet ^{19}F peak (-63.04 ppm with 2.30 Hz FWHM, **Figure S3**), we attribute these peaks to the presence of diastereomers, with both Ni^{2+} and donating N_{Bn} serving as stereogenic centers. A variable-temperature ^{19}F NMR experiment was performed to study the exchange of the two isomers and revealed only small changes in peak separation from 18.84 Hz at 8 ºC to 14.28 Hz at 80 ºC (**Figure S2**). This observation indicates an exchange rate of the two isomers much smaller than 20 s^{-1} as indicated by the NMR spectrum across all temperature. Due to vicinity of the two isomeric peaks, the ^{19}F MR relaxation times were measured by treating the peaks as one, giving a T_1 of 740 ms and a T_2 of 240 ms (**Table S1**). Both the longitudinal and transverse relaxation time are consistent with a diamagnetic Ni^{2+} complex.

Photo-irradiation of NiL_1

To investigate **NiL_1** as a spin-state switching agent, we irradiated an aqueous buffered solution of **NiL_1** at a light power of 3.5 mW/cm^2 and tracked the reaction progress via ^{19}F NMR. Prior to irradiation, only peaks from **NiL_1** were seen at -61.53 and -61.57 ppm (**Figure 2A**). Continuous irradiation resulted in generation of a new species with a characteristic broad peak at -24.76 ppm (FWHM = 22.7 Hz) and disappearance of the peaks from **NiL_1**. Both peaks of **NiL_1** declined simultaneously, consistent with them being diastereomers with the same chemical reactivity. The newly generated species was identified as **NiL_0** according to its ^{19}F NMR spectrum as well as high-resolution mass spectroscopy (**Figure 2A** and **S4**). T_1 and T_2 were measured for the newly emerged peak and both fall on the scale of tens of milliseconds (T_1 = 33 ms and T_2 = 15 ms), indicating the conversion from the diamagnetic **NiL_1** to the

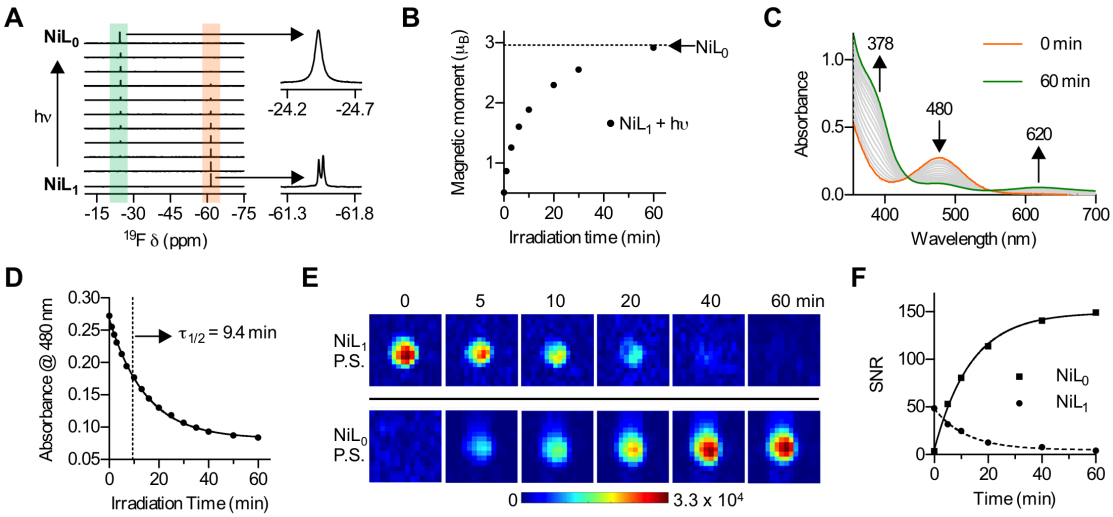

Figure 2. Characterization of the photochemical conversion of **NiL_1** to **NiL_0** in HEPES (50 mM, pH 7.4) at room temperature, assessed by (A) ^{19}F NMR (3.0 mM **NiL_1**), (B) magnetic moment measurement (5.0 mM **NiL_1**), (C) and (D) UV-*vis* absorption (1.0 mM **NiL_1**), (E) phantom ^{19}F MRI (4.0 mM **NiL_1**; upper panel, pulse sequence selected for **NiL_1**; lower panel, pulse sequence selected for **NiL_0**), and (F) phantom ^{19}F MRI signal-to-noise ratio analysis. **NiL_1** was irradiated by hand-held UV lamp at a power of 3.5 mW/cm^2 for an hour in total.

paramagnetic **NiL$_0$**. To further demonstrate the spin-state switching process, the magnetic moment after different durations of light-irradiation was assessed via Evans' method (**Figure 2B**). A gradual increase in magnetic moment was observed from 0.51 μ_B to 2.91 μ_B over an hour, with the final value approaching the magnetic moment of **NiL$_0$** (2.96 μ_B). The paramagnetism of Ni^{2+} in **NiL$_0$** was further validated by EPR spectroscopy in frozen aqueous solution; the EPR spectrum displayed a broad peak with a g factor of 1.99 (**Figure S5**).

The photochemical reaction kinetics were further evaluated through UV-vis absorption and ^{19}F NMR. During light irradiation, the characteristic absorbance of **NiL$_1$** at 480 nm in the UV-vis spectrum gradually decreased, with simultaneous increase in a shoulder at 378 nm and a broad peak at 620 nm (**Figure 2C**). Plotting the absorption at 480 nm against irradiation time exhibited a first-order decay with a half-life of 9.4 minutes (**Figure 2D**), consistent with previously reported reaction kinetics for photo-cleavage of ortho-nitrobenzyl-type groups.[23] Because only one event is observed, it is likely that upon cleavage of the nitrobenzyl moiety, the subsequent intramolecular coordination between phenolate and Ni^{2+} is too rapid to capture as a separate event by UV-vis spectroscopy. ^{19}F NMR-based quantification of the decay process of **NiL$_1$** closely mirrored the UV-vis absorption decay of **NiL$_1$**, affording the same half-life (9.5 minutes, **Figure S6**).

To evidence the application of **NiL$_1$** as a probe for ^{19}F MRI, we performed phantom imaging of an irradiated sample of **NiL$_1$** (**Figure 2E**). Given the distinction of both chemical shift and relaxation time between **NiL$_1$** and its irradiation product, **NiL$_0$**, we employed two different pulse sequences to selectively image **NiL$_1$** and **NiL$_0$** individually. A Rapid Acquisition with Relaxation Enhancement (RARE) pulse sequence with long echo time (TE = 40 ms) and long repetition time (TR = 1000 ms) was optimized for **NiL$_1$**, while **NiL$_0$** was best imaged with a RARE sequence with short echo time (TE = 2.0 ms) and short repetition time (TR = 55 ms). Consequently, there was zero cross-talk between the ^{19}F MR images of the two complexes. The initial signal for **NiL$_1$** (signal-to-noise ratio, SNR = 49.5) diminished over the course of irradiation (**Figure 2F**). Conversely, the signal intensity for **NiL$_0$** steadily increased, plateauing at SNR ~150 after irradiation for 60 minutes (**Figure 2F**). The higher SNR after irradiation points to the higher sensitivity of **NiL$_0$** compared to **NiL$_1$** as the shorter T_1 of **NiL$_0$** allows for increased acquisition replicates within a fixed imaging time. To quantify the sensitivity difference, we measured the limit-of-detection (LOD) of **NiL$_1$** and **NiL$_0$** (**Figure S7**), yielding values of 0.93 mM and 0.20 mM respectively in a ten-minute scan. This is consistent with reported LODs for diamagnetic and paramagnetic ^{19}F MR probes.[9a, 22a]

Structural insights for NiL$_0$ and NiL$_1$

To gain a deeper understanding of the spin-state difference between **NiL$_0$** and **NiL$_1$**, single crystals of **NiL$_0$** were obtained by slow evaporation of its solution in non-coordinating solvents (dichloroethane/pentene). As shown in **Figure 3A**, the Ni^{2+} center is five-coordinate with Ni-N(cyclam) bond lengths ranging from 2.014 Å to 2.085 Å and Ni-O (phenolate) bond distance of 1.999 Å, indicative of a high-spin Ni^{2+} complex. The strong donating phenolate caused the cyclam to adopt an unusual distorted *trans-II* configuration. While the acetate counterion participates in an extensive H-bonding network when **NiL$_0$** is in the solid state, no sixth ligand (e.g. acetate, H_2O) is observed in the primary coordination sphere of the metal center, consistent with a less flexible SB-Cyclam ligand where only intramolecular coordination to the Ni^{2+} center is allowed. To evaluate the coordination geometry of the Ni^{2+} center, Addison and Reedijk's τ_5 parameter was determined. An intermediate τ parameter of 0.51 indicated a structure that is right in-between square pyramidal and trigonal bipyramidal. This structural result is partly due to the presence of the chelating phenolate that "lifts" both the donating N_{Bn} and the Ni^{2+} center up from the average macrocyclic plane as defined by the other three SB-cyclam nitrogen donors (by 1.116 Å and 0.697 Å, respectively). Furthermore, the average distance between the fluorine atoms and Ni^{2+} center was 7.2 Å and assumed to be similar in solution due to the rigidity of the Ni-phenolate interactions. This distance falls within the effective range for PRE to result in shortened relaxation times of fluorine atoms.[24]

To correlate the solution structure of **NiL$_0$** with its solid-state structure, we measured the phenol pK_a of **NiL$_0$** to be 5.33 ± 0.01 in aqueous buffer using UV-vis (**Figure S8**). The acidic pK_a value indicates that in biologically relevant media at neutral pH, the phenol moiety will be largely deprotonated and will coordinate to Ni^{2+}. Further, the proton relaxivity r_1 measured in aqueous solution of NiL$_0$ was 0.020 ± 0.002 mM^{-1} s^{-1}, similar to octahedral Ni^{2+} complexes with no vacant site for water coordination.[25] In comparison, **NiL$_3$**, the cyclam analogue of **NiL$_0$** in which there is no side-bridge, can coordinate water to form a 6-coordinate species[26] and displayed a proton relaxivity of 0.13 ± 0.01 mM^{-1} s^{-1}, 6.5x larger than **NiL$_0$**. These results support a five-coordinate structure of **NiL$_0$** in aqueous solution with no bound H_2O, facilitated by the presence of the cyclam side-bridge. The defined solution structure of **NiL$_0$**, as suggested by its single ^{19}F NMR peak, brings a significant advantage over chemical-shift based lanthanide probes whose MR signals are diluted by the presence of multiple isomers in aqueous solution.[27]

We performed DFT calculations on a level of B3LYP/6-31G(d,p) to understand the electronic structure of **NiL$_0$**. The optimized structure of **NiL$_0$** well mimics its X-ray structure; superimposed structures are shown in **Figure S9**, with τ_5 = 0.53 for the optimized structure. The calculated d-orbital splitting (**Figure 3B**) indicates that the strong coordination between the phenolate and Ni^{2+} raises the energy levels of the d_{xy} and d_{z^2} orbitals close to the $d_{x^2-y^2}$ resulting in a high-spin Ni^{2+} center (S = 1). In this calculation, the difference in the energy of the filled d_{xy} and a

10.1002/anie.202010587
WILEY-VCH

RESEARCH ARTICLE

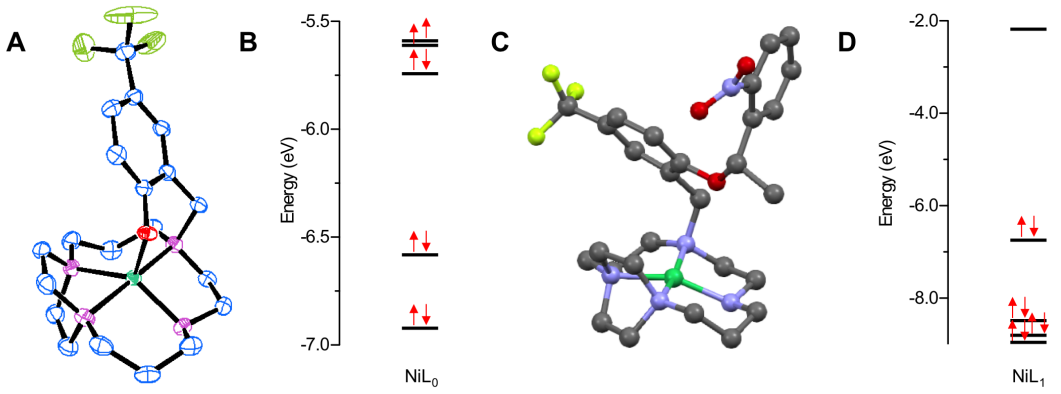

Figure 3. (A) ORTEP representation of **NiL₀** from a square pyramidal view. Thermal ellipsoid plot at 50% probability level. Solvent molecules, counter anion (acetate), and hydrogen atoms are omitted for clarification. (B) Calculated d-orbital diagram and d^8-electron fillings of **NiL₀**. (C) Optimized structure of **NiL₁** by DFT calculations. Bond lengths of Ni-N_{cyclam} are 1.97, 1.94, 1.95, and 1.95 Å. (D) Calculated d-orbital diagram and d^8-electron fillings **NiL₁**.

half-filled $d_{x^2-y^2}$ orbital is small (0.13 eV), indicating there is a low-lying excited state that could couple with the ground state to generate large zero-field splitting (*D*) and introduce high magnetic anisotropy.[28] High-spin Ni^{2+} coordinated in trigonal-bipyramid geometry has been shown to induce large negative *D* values in design of single-molecular magnets.[29] Compared to the chemical shifts of **L₀** (-60.69 ppm) and **NiL₁** (-61.01 ppm), **NiL₀** displayed a peak at -24.76 ppm, a downfield shift by more than 35 ppm (**Figure S10**). Moreover, the diamagnetic Zn^{2+} analogue of **NiL₀** (**ZnL₀**, -60.45 ppm) only showed a 0.24 ppm downfield shift comparing to the ligand **L₀** (**Figure S10**), excluding the effect of the metal Lewis acidity on the ^{19}F chemical shift of the -CF_3 group. These observations emphasize the pivotal role of Ni^{2+}-phenolate coordination in inducing magnetic anisotropy of the paramagnetic Ni^{2+} center and strengthening through-bond contact between Ni^{2+} and ^{19}F. Both the contact shift and pseudocontact shift contribute to the large downfield shift of the ^{19}F NMR resonance in **NiL₀**.

The DFT-optimized structure of **NiL₁** clearly showed shorter bond lengths of Ni^{2+}-N(cyclam) (c.a. 1.94 Å to 1.97 Å), characteristic of a diamagnetic Ni^{2+} center (**Figure 3C**). The phenol-ether oxygen atom lies 3.75 Å away from Ni^{2+} that precludes its coordination and therefore, Ni^{2+} is best described as a distorted square-planar coordination geometry. Correspondingly, the d-orbital splitting diagram of **NiL₁** exhibits a high-lying unfilled $d_{x^2-y^2}$ orbital that is well above the closest d_{z^2} orbital (separated by 4.56 eV) and, consequently, all the d-electrons are paired, resulting in a diamagnetic **NiL₁** (**Figure 3D**).

Photo-conversion of NiL₁ to NiL₀ in cell culture

Prior to cellular testing, we monitored the stability of **NiL₁** and **NiL₀** in presence of bio-available metal ions (100 mM KNO_3, 100 mM NaCl, 10 mM $MgCl_2$, 10 mM $CaCl_2$, and 10 mM $ZnCl_2$) using UV-vis absorption (**Figure S11**). After 24-hour incubation, the characteristic d-d bands of both complexes remained nearly unchanged (λ_{max} = 452 nm for **NiL₁** and λ_{max} = 381, 472, and 616 nm for **NiL₀**), indicating little to no trans-metalation occurred. Further, this indicated that even in the presence of excess Cl^- or NO_3^-, the primary coordination sphere of the Ni^{2+} did not change in either complex. While $[Ni(cyclam)]^{2+}$ is well known for its extreme kinetic stability,[30] the double ethylene bridge present in the ligand framework likely reduces the flexibility of macrocycle and further enhances the inertness of the complexes.

As a step towards bio-application of this coordination-based strategy, we studied the photochemical conversion of **NiL₁** to **NiL₀** in the context of live cells. HeLa cells were incubated with **NiL₁**, cell pellets were collected and ^{19}F NMR and MRI were taken before and after light irradiation (λ = 365 nm). Interestingly, before irradiation, the ^{19}F NMR spectrum was silent (**Figure 4**). The disappearance of the **NiL₁** signal is likely caused by the interaction between the hydrophobic ortho-nitrophenyl group in the complex and cellular proteins. Indeed, the ^{19}F NMR spectrum of **NiL₁** in the presence of fetal bovine serum displayed a much broader and featureless peak (FWHM = 123 Hz, **Figure S12**) compared to the peaks seen in aqueous buffer (FWHM = 5.70, 5.38 Hz). Signal quenching (significant T_2 decrease) because of hydrophobic interactions has been reported for analogous metal-cyclen complexes.[31] After light irradiation, a strong signal was observed at –24.89 ppm (FWHM = 25.38 Hz), corresponding to the expected formation of **NiL₀**, which was sharper and better mimicked the peak observed in aqueous HEPES buffer in this case (FWHM = 32.2 Hz in FBS versus FWHM = 21.2 Hz in HEPES, **Figure S12**). ^{19}F MR phantom imaging was performed by selectively observing the signal from **NiL₀** due to its lower detection limit and less hydrophobic-interaction-induced signal loss. As shown in **Figure 4**, only background signal was detected for the cell pellets before irradiation (SNR 2.6, 30-minute scan). However, after one-hour light exposure, a moderate signal could be observed with an SNR of 6.5. These imaging results

10.1002/anie.202010587

demonstrate the potential application of Ni^{2+} SB-Cyclam-based complexes for ^{19}F MR sensing in complex cellular environments.

In vitro enzymatic cleavage of NiL$_2$

The promising results of implementing a spin-state switching imaging agent in cells using highly controlled chemistry alluded to the potential of adapting this platform to detect biological activity, such as the activity of enzymes. As an example, we prepared **NiL$_2$** that incorporates a galactose moiety for sensing the activity of β-galactosidase (β-Gal), an exoglycosidase that hydrolyzes the β-glycosidic bond. β-Gal was chosen because it has been widely engineered as a co-expressed reporter protein for human-made constructs in mammalian cells and in organisms and has been used in cellular and *in vivo* imaging.[32] In our study, we designed **NiL$_2$** to undergo a self-immolative process in response to β-Gal to generate **NiL$_0$** for ^{19}F MR-based sensing.

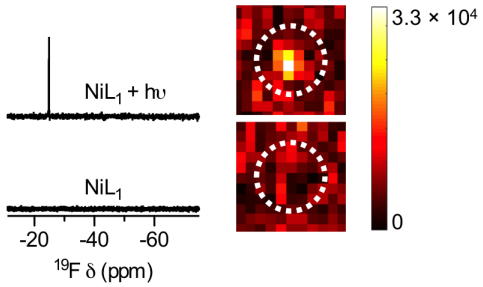

Figure 4. Detection of photoactivation of **NiL$_1$** in HeLa cells through ^{19}F NMR and ^{19}F MRI. (Left) ^{19}F NMR spectra at 9.4 T of HeLa cell pellets labeled with 1 mM NiL_1 before (bottom spectrum) and after (top spectrum) photo-irradiation. (Right) ^{19}F MRI imaging on a 7T scanner of **NiL$_0$** in HeLa cell pellets before and after photo-irradiation.

Similar to **NiL$_1$**, **NiL$_2$** is diamagnetic in aqueous buffer, displaying a sharp singlet peak with long ^{19}F relaxation times (T_1 = 790 ms, T_2 = 320 ms), and a d-d transition band at 480 nm with ε = 2.8x10^2 $M^{-1}cm^{-1}$ in its UV-vis absorption spectrum (**Figure 5A and S1**). In the presence of β-Gal, the NMR peak for **NiL$_2$** at -61.42 ppm declined while the peak for **NiL$_0$** at -24.76 ppm gradually increased. The efficient conversion of **NiL$_2$** to **NiL$_0$** via β-Gal was confirmed by a test trial between 1.5 μmol **NiL$_2$** and 3 U enzyme, where >95% conversion was observed after 40 minutes (**Figure 5A**). No cleavage was found when **NiL$_2$** was incubated with heat-inactivated β-Gal (**Figure S13**).

Along with the formation of **NiL$_0$**, enzymatic cleavage of **NiL$_2$** produced an intense yellow color, corresponding to the absorption of 4-(hydroxymethyl)-2-nitrophenate motif. Its high molar absorptivity (~10^3) allows analysis of β-Gal enzyme kinetics through monitoring the absorption increase at 403 nm. A fixed amount of β-Gal (1.5 U) was incubated with a buffered solution of **NiL$_2$** at 37 ºC and absorption at 403 nm was recorded over an 800-second period (**Figure S14**). At different **NiL$_2$** concentrations, all the absorption increases displayed a first-order exponential increase. The enzyme kinetic parameters were further calculated according to Lineweaver-Burk reciprocal plot, which returned a Michaelis constant K_m of (9.7 ± 1.4) x10^2 μM and a catalytic rate k_{cat} of 15 ± 2 s^{-1} (**Figure 5B**). These results fall on the same order but suggest slower kinetics compared to published results[33] on o-nitrophenyl β-D-galactoside, a standard substrate for spectroscopic detection of β-Gal activity, due partly to the larger size of the **NiL$_2$** complex. Regardless, **NiL$_2$** appeared to be an efficient substrate for β-Gal.

To demonstrate the use of **NiL$_2$** for probing β-Gal activity by ^{19}F MRI, we cultured **NiL$_2$** with regular and heat-inactivated β-Gal under the same conditions used for NMR experiments (**Figure 5C**). As expected, **NiL$_2$** in absence of β-Gal or in presence of heat-inactivated β-Gal did not show any conversion into **NiL$_0$**. When **NiL$_2$** is mixed with active β-Gal, a time-course phantom ^{19}F MRI with 5-minute interval well mimicked the progress of β-Gal-catalyzed cleavage as seen by ^{19}F NMR (**Figure S15**), with signal enhancement for **NiL$_0$** over a period of 40 minutes. While the signal for **NiL$_2$** almost faded away after 20 minutes of incubation, **NiL$_0$** signal increases were still observed, consistent with the higher sensitivity of the paramagnetic **NiL$_0$** compared to the diamagnetic **NiL$_2$**.

Detection of β-Gal enzymatic activity at a cellular level

We further studied the capability of **NiL$_2$** in detecting cellular β-Gal activity via genetically encoded expression of β-Gal in HEK 293T cells using the immediate-early promoter from cytomegalovirus (pcDNA3.1/His/LacZ).[32b] **NiL$_2$** was then co-cultured with HEK 293T cells for two hours, and the media was collected and subjected to ^{19}F NMR/MRI analysis. As shown in **Figure 5D**, ^{19}F NMR clearly indicated the conversion of **NiL$_2$**, with a characteristic singlet peak at -24.78 ppm assigned to **NiL$_0$**. At a cell population of ~1.0 million and a **NiL$_2$** dosage of 1.0 μmol, cell uptake of **NiL$_2$** was determined to be 1.5 ± 0.1 fmol/cell and the conversion of **NiL$_2$** was 70 ± 10 %, a sign of efficient cell uptake, enzymatic transformation, and trans-membrane diffusion of the cleaved product (**NiL$_0$**). On the other hand, when **NiL$_2$** was incubated with cells not expressing β-Gal, only slight conversion (c.a. 8.0 ± 0.5 %) was noticed. Similar result was observed when **NiL$_2$** itself was incubated in cell culture media under the same conditions. To explain this "background" reactivity, we further tested the stability of **NiL$_2$** in presence of glutathione (reduced type). The moderate reactivity of **NiL$_2$** as observed (9.9 % conversion of **NiL$_2$**, **Figure S16**) indicates that free thiol-groups could cleave the galactose side chain and compromise the stability of **NiL$_2$** in culture media. We note, however, due to the stochiometric nature and slow kinetics of the reaction between **NiL$_2$** and thiol groups, our probe is still favorable for probing the catalytic activity of β-Gal in biological systems, as seen by around 8-fold enhancement of **NiL$_2$**

10.1002/anie.202010587

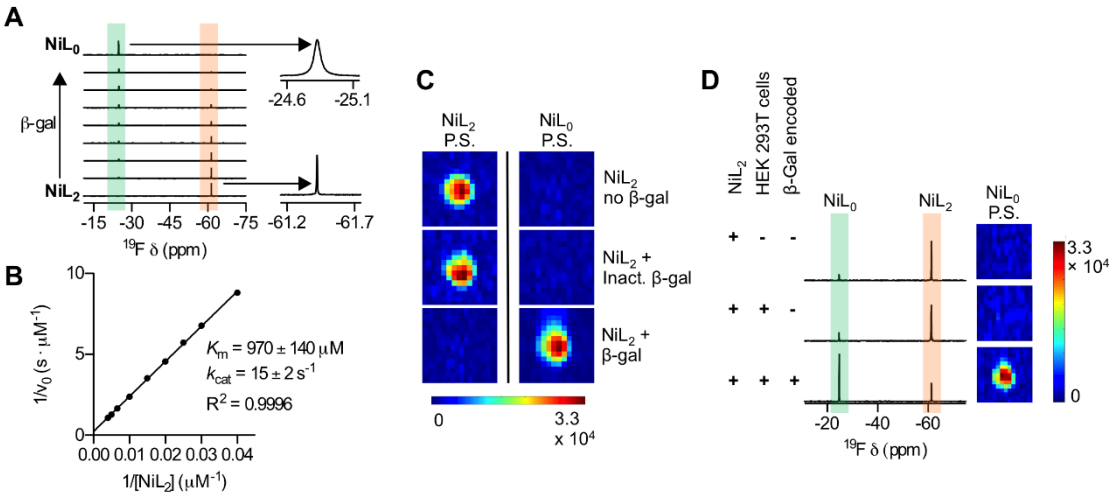

Figure 5. (A) Detection of *in vitro* β-galactosidase activity by **NiL₂** through ^{19}F NMR. (B) Lineweaver-Burk reciprocal plot for determination of enzyme kinetics. Michaelis constant K_m and k_{cat} were found to be (9.7 ± 1.4) x10^2 μM and 15 ± 2 s^{-1}, respectively. (C) Phantom ^{19}F MRI of *in vitro* β-Gal activity at 7 T. Pulse sequences were selected for **NiL₂** and **NiL₀**, respectively. (D) Detection of β-Gal activity in HEK 293T cells through ^{19}F NMR and ^{19}F MRI using **NiL₂**. A RARE pulse sequence selective for **NiL₀** was applied for ^{19}F MRI.

conversion in presence versus in absence of cellular β-Gal. ^{19}F MRI was further conducted to demonstrate the use **NiL₂** in sensing activity of cellular β-Gal (**Figure 5D**). **NiL₀** was selectively imaged using a RARE pulse sequence due to its lower limit-of-detection. Without encoded expression of β-Gal, the low conversion of **NiL₂** could not be visualized and the signal of **NiL₀** was on the level of noise (SNR ~ 3). When β-Gal was present, a strong signal was tracked, giving an SNR of 26.6. The sharp contrast between images well correlated with the observation in ^{19}F NMR and emphasized the viability of using ^{19}F MR imaging to study cellular activities in a "turn-on" manner via tuning the spin-state of a Ni^{2+} center.

Conclusion

Taken together, we have established Ni^{2+} SB-Cyclam as a versatile spin-state switching platform for designing aqueous ^{19}F MR probes for both *in vitro* and cellular applications. Our mechanism relies on distinct changes in the Ni^{2+} coordination environment that trigger changes in the electronic structure of the metal center, converting it from a low-spin S=0 species to a high spin S=1 species with low-lying excited electronic states. This change in coordination also modulates the through bond interactions between the metal and the ^{19}F reporter. Importantly, the product paramagnetic Ni-phenolate species exhibits large changes in ^{19}F chemical shift relative to the initial probe, resulting from modulation of both contact and pseudocontact shift effects. The distinction in magnetic properties between high-spin and low-spin fluorinated Ni^{2+} complexes allows NMR/MRI tracking of both species separately, making it possible to monitor reactions with this complex in biological contexts. The probes reported herein are limited, however, due to their low ^{19}F content that will limit the ability to detect their signal in an efficient manner *in vivo*. Ongoing efforts include developing probes that have higher SNR, require shorter scan times, and exhibit improved pharmacokinetics in order to better facilitate *in vivo* applications. This represents a new platform for monitoring biochemical events that should be readily adapted for the detection of a range of analytes in biological contexts including small molecules and enzymes that are of interest to medical diagnostics.

Experimental Section

Photo-irradiation assay of NiL₁

NiL₁ was dissolved in HEPES buffer (pH 7.4, 50 mM, added 100 mM KNO_3) and irradiated from the side by hand-held UV lamp at 365 nm at a power of 3.5 mW/cm^2. Spectroscopic measurement (including UV-vis absorption, ^{1}H NMR, and ^{19}F NMR) was performed at following indicated time points within an overall photo-irradiation time of an hour: UV-vis absorption spectrum: 0, 1, 2, 3, 5, 7, 10, 13, 16, 20, 25, 30, 35, 40, 50, and 60 min; ^{1}H NMR spectrum: 0, 1, 3, 6, 10, 20, 30, 60 min; ^{19}F NMR spectrum: 0, 1, 3, 6, 10, 15, 20, 30, 40, 60 min.

Enzymatic assay of NiL₂

NiL₂ was dissolved in HEPES buffer (50 mM, pH 7.4, added 10 mM $MgCl_2$ and 100 mM KCl) and was cultured with β-galactosidase at an activity dosage of 2U/μmol **NiL₂**. ^{19}F NMR spectrum was taken at 0, 5, 7.5, 10, 15, 20, 30 and 40-min time point to evaluate the enzymatic conversion of **NiL₂** to **NiL₀**.

To assess the enzyme kinetics, a series of parallel enzymatic reactions were performed at 310 K with **NiL₂** concentration from 25 μM to 250 μM and a fixed β-gal activity of 1.5 U. The reaction progress was tracked by UV-vis absorption at 403 nm for a duration of 800 seconds, and this time-dependent absorption enhancement was fitted to first-order kinetics for estimation of the initial reaction rate v_0. Michaelis constant K_m and catalytic

rate k_{cat} were further calculated according to Lineweaver-Burk reciprocal plot[3] ($1/v_0$ *versus* $1/[\mathbf{NiL_2}]$).

Acknowledgements

This research was supported by funding from the Welch Foundation (F-1883) and the National Science Foundation (CHE-1945401). We gratefully acknowledge Prof. Andrew Ellington and Shaunak Kar for helpful discussions regarding cellular enzyme expression experiments. MR phantoms were acquired at the Biomedical Imaging Center at the Dell Medical School at UT Austin.

Keywords: nickel •fluorine • magnetic resonance spectroscopy and imaging • coordination chemistry • biosensing

[1] a) D. N. Woodruff, R. E. P. Winpenny, R. A. Layfield, Chem. Rev. 2013, 113, 5110-5148; b) G. A. Craig, M. Murrie, Chem. Soc. Rev. 2015, 44, 2135-2147.

[2] a) R. B. Lauffer, Chem. Rev. 1987, 87, 901-927; b) J. Wahsner, E. M. Gale, A. Rodríguez-Rodríguez, P. Caravan, Chem. Rev. 2019, 119, 957-1057; c) A. Gupta, P. Caravan, W. S. Price, C. Platas-Iglesias, E. M. Gale, Inorg Chem 2020, 59, 6648-6678.

[3] a) G. Angelovski, Angew. Chem. Int. Ed. Engl. 2016, 55, 7038-7046; b) M. C. Heffern, L. M. Matosziuk, T. J. Meade, Chem. Rev. 2014, 114, 4496-4539; c) E. L. Que, C. J. Chang, Chem. Soc. Rev. 2010, 39, 51-60; d) L. M. De Leon-Rodriguez, A. J. M. Lubag, C. R. Malloy, G. V. Martinez, R. J. Gillies, A. D. Sherry, Acc. Chem. Res. 2009, 42, 948-957.

[4] J. Ruiz-Cabello, B. P. Barnett, P. A. Bottomley, J. W. M. Bulte, NMR Biomed. 2011, 24, 114-129.

[5] I. Tirotta, V. Dichiarante, C. Pigliacelli, G. Cavallo, G. Terraneo, F. B. Bombelli, P. Metrangolo, G. Resnati, Chem. Rev. 2015, 115, 1106-1129.

[6] a) H. Chen, S. Viel, F. Ziarelli, L. Peng, Chem. Soc. Rev. 2013, 42, 7971-7982; b) S. L. Cobb, C. D. Murphy, J. Fluorine Chem. 2009, 130, 132-143; c) K. L. Peterson, K. Srivastava, V. C. Pierre, Front. Chem. 2018, 6; d) E. N. G. Marsh, Y. Suzuki, ACS Chem. Biol. 2014, 9, 1242-1250; e) D. Xie, M. Yu, R. T. Kadakia, E. L. Que, Acc Chem Res 2020, 53, 2-10.

[7] a) K. Akazawa, F. Sugihara, T. Nakamura, S. Mizukami, K. Kikuchi, Bioconjugate Chemistry 2018, 29, 1720-1728; b) S. Mizukami, R. Takikawa, F. Sugihara, M. Shirakawa, K. Kikuchi, Angew. Chem. Int. Ed. Engl. 2009, 48, 3641-3643; c) S. Mizukami, R. Takikawa, F. Sugihara, Y. Hori, H. Tochio, M. Wälchli, M. Shirakawa, K. Kikuchi, J. Am. Chem. Soc. 2008, 130, 794-795.

[8] H. Chen, X. Tang, X. Gong, D. Chen, A. Li, C. Sun, H. Lin, J. Gao, Chem Commun (Camb) 2020, 56, 4106-4109.

[9] a) M. Yu, B. S. Bouley, D. Xie, J. S. Enriquez, E. L. Que, J. Am. Chem. Soc. 2018, 140, 10546-10552; b) M. Yu, D. Xie, K. P. Phan, J. S. Enriquez, J. J. Luci, E. L. Que, Chem. Commun. 2016, 52, 13885-13888.

[10] a) R. T. Kadakia, D. Xie, D. Martinez, M. Yu, E. L. Que, Chem. Commun. 2019, 55, 8860-8863; b) J. S. Enriquez, M. Yu, B. S. Bouley, D. Xie, E. L. Que, Dalton Trans. 2018, 47, 15024-15030; c) D. Xie, S. Kim, V. Kohli, A. Banerjee, M. Yu, J. S. Enriquez, J. J. Luci, E. L. Que, Inorg. Chem. 2017, 56, 6429-6437; d) D. Xie, T. L. King, A. Banerjee, V. Kohli, E. L. Que, J. Am. Chem. Soc. 2016, 138, 2937-2940; e) R. T. Kadakia, D. Xie, H. Guo, B. Bouley, M. Yu, E. L. Que, Dalton Trans 2020.

[11] L. A. Basal, M. D. Bailey, J. Romero, Meser M. Ali, L. Kurenbekova, J. Yustein, R. G. Pautler, M. J. Allen, Chem. Sci. 2017, 8, 8345-8350.

[12] V. V. Smirnov, E. K. Woller, S. G. DiMagno, Inorg. Chem. 1998, 37, 4971-4978.

[13] A. I. Gaudette, A. E. Thorarinsdottir, T. D. Harris, Chem. Commun. 2017, 53, 12962-12965.

[14] a) K. H. Chalmers, E. De Luca, N. H. M. Hogg, A. M. Kenwright, I. Kuprov, D. Parker, M. Botta, J. I. Wilson, A. M. Blamire, Chem. Eur. J. 2010, 16, 134-148; b) A. M. Kenwright, I. Kuprov, E. De Luca, D. Parker, S. U. Pandya, P. K. Senanayake, D. G. Smith, Chem. Commun. 2008, 2514-2516; c) M. Yu, D. Xie, R. T. Kadakia, W. Wang, E. L. Que, Chem Commun (Camb) 2020, 56, 6257-6260; d) G. Gambino, T. Gambino, R. Pohmann, G. Angelovski, Chem Commun (Camb) 2020, 56, 3492-3495.

[15] F. Meyer, H. Kozlowski, in Comprehensive Coordination Chemistry II (Eds.: J. A. McCleverty, T. J. Meyer), Pergamon, Oxford, 2003, pp. 247-554.

[16] a) J. Blahut, K. Bernášek, A. Gálisová, V. Herynek, I. Císařová, J. Kotek, J. Lang, S. Matějková, P. Hermann, Inorg. Chem. 2017, 56, 13337-13348; b) J. Blahut, P. Hermann, A. Gálisová, V. Herynek, I. Císařová, Z. Tošner, J. Kotek, Dalton Trans. 2016, 45, 474-478.

[17] a) M. Dommaschk, M. Peters, F. Gutzeit, C. Schütt, C. Näther, F. D. Sönnichsen, S. Tiwari, C. Riedel, S. Boretius, R. Herges, J. Am. Chem. Soc. 2015, 137, 7552-7555; b) S. Thies, H. Sell, C. Schütt, C. Bornholdt, C. Näther, F. Tuczek, R. Herges, J. Am. Chem. Soc. 2011, 133, 16243-16250.

[18] X. Liang, P. J. Sadler, Chem Soc Rev 2004, 33, 246-266.

[19] K. P. Wainwright, Inorg. Chem. 1980, 19, 1396-1398.

[20] L. Fabbrizzi, F. Foti, M. Licchelli, A. Poggi, Inorg. Chem. 2002, 41, 4612-4614.

[21] E. Kimura, T. Koike, K. Uenishi, M. Hediger, M. Kuramoto, S. Joko, Y. Arai, M. Kodama, Y. Iitaka, Inorg. Chem. 1987, 26, 2975-2983.

[22] a) D. Xie, L. E. Ohman, E. L. Que, Magn. Reson. Mater. Phys., Biol. Med. 2019, 32, 89-96; b) E. Kimura, T. Koike, H. Nada, Y. Iitaka, Inorg. Chem. 1988, 27, 1036-1040.

[23] P. Klán, T. Šolomek, C. G. Bochet, A. Blanc, R. Givens, M. Rubina, V. Popik, A. Kostikov, J. Wirz, Chem. Rev. 2013, 113, 119-191.

[24] I. Bertini, C. Luchinat, G. Parigi, E. Ravera, in NMR of Paramagnetic Molecules (Second Edition) (Eds.: I. Bertini, C. Luchinat, G. Parigi, E. Ravera), Elsevier, Boston, 2017, pp. 175-253.

[25] A. O. Olatunde, S. J. Dorazio, J. A. Spernyak, J. R. Morrow, J. Am. Chem. Soc. 2012, 134, 18503-18505.

[26] N. Sengottuvelan, D. Saravanakumar, M. Kandaswamy, Inorg. Chem. Comm. 2005, 8, 297-300.

[27] A. C. Harnden, D. Parker, N. J. Rogers, Coord. Chem. Rev. 2019, 383, 30-42.

[28] S. Gomez-Coca, E. Cremades, N. Aliaga-Alcalde, E. Ruiz, J. Am. Chem. Soc. 2013, 135, 7010-7018.

[29] K. E. R. Marriott, L. Bhaskaran, C. Wilson, M. Medarde, S. T. Ochsenbein, S. Hill, M. Murrie, Chem. Sci. 2015, 6, 6823-6828.

[30] E. J. Billo, Inorg. Chem. 1984, 23, 236-238.

[31] K. Srivastava, E. A. Weitz, K. L. Peterson, M. Marjańska, V. C. Pierre, Inorg. Chem. 2017, 56, 1546-1557.

[32] a) J.-X. Yu, V. D. Kodibagkar, R. R. Hallac, L. Liu, R. P. Mason, Bioconj. Chem. 2012, 23, 596-603; b) S. Mizukami, H. Matsushita, R. Takikawa, F. Sugihara, M. Shirakawa, K. Kikuchi, Chem. Sci. 2011, 2, 1151-1155; c) J. L. Major, T. J. Meade, Acc. Chem. Res. 2009, 42, 893-903.

[33] S. Jambovane, E. C. Duin, S.-K. Kim, J. W. Hong, Anal. Chem. 2009, 81, 3239-3245.

10.1002/anie.202010587

WILEY-VCH

RESEARCH ARTICLE

Entry for the Table of Contents

RESEARCH ARTICLE

Text for Table of Contents

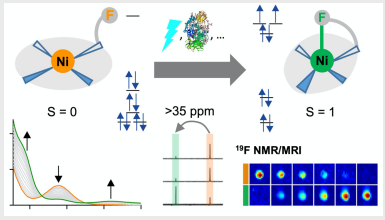

*Da Xie, Meng Yu, Zhu-Lin Xie, Rahul T. Kadakia, Chris Chung, Lauren Ohman, Kamyab Javanmardi, Emily L. Que**

Page No. – Page No.

Versatile Nickel (II) Scaffolds as Coordination-Induced Spin-State Switches for ^{19}F Magnetic Resonance-Based Detection